RSC Advances

PAPER

View Article Online
View Journal | View Issue

Cite this: *RSC Adv.*, 2026, **16**, 29981

Decoding the hydrogen storage and functional properties of $MgBH_3$ (B = Mo and In) *via* first-principles simulations

Md Shahazan Parves, [a] Md. Hasan Mia, *[bc] Omar Alsalmi[d] and Md. Zahid Hasan *[b]

This present study presents a complete first-principles investigation of the structural, hydrogen storage, optoelectronic, mechanical, and thermodynamic properties of $MgBH_3$ (B = Mo, In). Cubic phase structural stability was determined by formation energies, Goldschmidt tolerance factors, and octahedral factors. Hydrogen storage capacities were calculated as 2.45 wt% for $MgMoH_3$ and 2.13 wt% for $MgInH_3$, indicating reasonable desorption suitable for real-world energy storage. Electronic structure calculations (GGA-PBE) determine metallic conductivity as a result of valence and conduction band overlap. Optical analyses show that the high refractive index and strong absorption of $MgBH_3$, combined with their metallic nature, ensure efficient charge transport and lattice stability. Mechanical stability is confirmed by the elastic constants satisfying Born's criteria. This stability, coupled with their distinct ductile nature, ensures robust structural integrity and prevents microcracking, making repeated hydrogen cycling highly stable. Strong elastic anisotropy is indicative of the directional dependence of hydride perovskites. Thermodynamic assessment: Debye temperature, lattice and minimum thermal conductivities, and Grüneisen parameter offer insight into phonon transport and heat capacity, confirming their utility as thermal barrier coatings at high temperatures. In short, $MgBH_3$ (B = Mo, In) hydrides are multifunctional materials exhibiting moderate hydrogen-storage capability, robust mechanical stability, favorable thermal-management characteristics, and distinct dielectric and metallic optical responses.

Received 15th May 2026
Accepted 22nd May 2026

DOI: 10.1039/d6ra04227a

rsc.li/rsc-advances

1. Introduction

As the global population continues to rise, so too has the quantity of energy used worldwide. This increase stems from the increased energy needs caused by technical progress and advances in science aimed at providing modern amenities for society. Fossil fuels, which are non-renewable resources that take a long time to replenish or return to their original state, provide a sizable portion of the world's energy.[1] Since carbon-based combustion and the reliance on inefficient fossil fuels have been linked to nearly a 35% increase in CO_2 emissions, hydrogen is gaining attention as a promising alternative source of energy due to its abundance, non-toxicity, high efficiency, and long-term sustainability.[2] Hydrogen-based energy systems were launched after the global oil crisis of the 1970s, and they have the potential to revolutionize the transportation and power engineering industries.[3] As the most abundant element in the universe and the lightest fuel available, hydrogen is recognized as a highly effective energy carrier,[4] with certain metal hydride perovskites demonstrating efficiency improvements from around 3.8% to above 20%.[5] One of the first uses of hydrogen as a reserve fuel was the first human voyage to the moon, and several nations are now using it for transportation.[6] Materials that can store hydrogen at room temperature and pressure while attaining high volumetric and gravimetric hydrogen densities are the subject of the current study.[7] The 2019 launch of Hyundai's Nexo fuel cell vehicle, which sold over 1000 units in South Korea and demonstrated the growing market acceptability of hydrogen-based transportation options, is a concrete example of this expanding trend toward hydrogen utilization commercially.[8] High volumetric and gravimetric ratios, quick reaction kinetics, robust mechanical stability, and the capacity to release hydrogen under normal operating conditions are all expected to be characteristics of ideal energy storage materials.[9] To industrially implement hydrogen as a sustainable energy source, a range of technical challenges must be addressed and overcome.[10] Hydrogen has been increasingly adopted worldwide as an alternative clean fuel because it generates energy without producing carbon dioxide, with water being its only by-product, free from pollutants, ozone-depleting

[a]*Graduate School of Environmental Engineering, The University of Kitakyushu, 1-1 Hibikino, Kitakyushu 808-0135, Japan*

[b]*Materials Research and Simulation Lab, Department of Electrical and Electronic Engineering, International Islamic University Chittagong, Kumira, Chittagong, 4318, Bangladesh. E-mail: mdhasan111.ru@gmail.com; zahidhasan.02@gmail.com*

[c]*Department of Computer and Communication Engineering, International Islamic University Chittagong, Kumira, Chittagong, 4318, Bangladesh*

[d]*Department of Physics, College of Science, Umm Al-Qura University, Makkah 21955, Saudi Arabia*

agents, or harmful synthetic chemicals.[11] However, storing hydrogen efficiently continues to be a significant challenge compared to conventional methods. Compression increases safety concerns and restricts the amount of hydrogen that can be contained under high pressure,[12] whereas liquefaction, despite saving storage space, raises the risks of evaporation and emission losses,[13] making the search for safer and more cost-effective storage materials crucial.[14] Extensive experimental and theoretical studies in recent years have evaluated their potential for efficient hydrogen storage.[15] For these materials to be useful in the long run, they must fulfill a number of important criteria.[16] ABH_3 compounds can generally be classified according to the elements they contain: an A-site element from group I or II of the periodic table and a B-site element from the transition metal group, which was first discovered by German scientist Gustav Rose in the Ural Mountains in 1839.[17] In the general ABX_3 formula, A denotes an alkali metal, B a transition metal, and X represents oxygen or a halogen element commonly forming a cubic lattice within the $Pm\bar{3}m$ crystallographic space group.[18]

According to research, oxides rather than hydrides are frequently formed as a result of hydrogen's poor stability and cation restrictions. Nonetheless, lightweight metal hydrides have garnered interest because of their high gravimetric densities, reversible absorption/desorption behavior, and exceptional thermal stability, which make them attractive options for real-world hydrogen storage applications.[19] However, some inherent characteristics, such as high formation enthalpy, strong thermodynamic stability, sluggish kinetics of hydrogen absorption and desorption, and vulnerability to oxidation in air, restrict the practical application of magnesium hydrides.[20]

$CaXH_3$ (X = Mn, Fe, and Co) hydride-type perovskites have been studied in the past to assess their feasibility for storing hydrogen.[21] Theoretical investigations point out that $MgBH_3$ and $MgNH_3$ perovskite materials can gain hydrogen storage levels well above the Department of Energy's (DOE) target of 5.5 wt% for onboard applications, achieving roughly 15.4 wt% and 14.9 wt% respectively.[22] Magnesium-based perovskite hydrides can also be prepared experimentally using a variety of synthesis approaches, including solution-based techniques, ball milling, and conventional solid-state methods. Siddique *et al.*[23] also reported that $AeVH_3$ (Ae = Be, Mg, Ca, Sr) perovskite hydrides exhibit ionic bonding with no bandgap, possess gravimetric hydrogen storage capacities of 3.45, 3.52, 3.60, and 3.65 wt% for $BeVH_3$, $MgVH_3$, $CaVH_3$, and $SrVH_3$, respectively.

The growing need for effective hydrogen storage and sophisticated optoelectronic materials underscores the need to explore additional members of this material class, even in spite of significant progress in the study of magnesium-based perovskites. The current study offers a first-principles density functional theory (DFT) investigation of the structural, elastic, thermodynamic, optoelectronic, and hydrogen storage features of $MgBH_3$ (B = Mo, In), motivated by its unique physical properties and exciting potential uses. The goal of this theoretical investigation is to establish a thorough understanding of these materials and evaluate their applicability for real-world energy storage and electronic device applications.

2. Computational details

In this investigation, the CASTEP package was utilized, which is draws on a plane-wave pseudopotential formalism for total energy calculations, making it suitable for reliable simulations of material attributes. Our study ensured that the generalized gradient approximation (GGA), specifically the Perdew Burke Ernzerhof (PBE) functional[24] and its revised form PBEsol,[25] reproduced the lattice constants and unit-cell volumes of $MgBH_3$ with greater precision than the local density approximation (LDA), and were in closer agreement with experimental findings. Hence, the PBE scheme was chosen for all subsequent computations. The geometric optimization of the crystal structures was carried out using the Broyden Fletcher Goldfarb Shanno (BFGS) minimization algorithm,[26] confirming that the most energetically stable configuration of $MgBH_3$ (X = Mo, In) was acquired. The plane-wave basis set cut-off energy and Brillouin zone sampling were carefully optimized through convergence tests of total energy, atomic forces, and stress to ensure computational accuracy. A cut-off energy of 500 eV and a $6 \times 6 \times 6$ Monkhorst–Pack k-point grid were found to provide well-converged results for both hydrides. The electronic minimization was performed using self-consistent field (SCF) iterations with a total energy convergence tolerance of 2.0×10^{-5} eV/atom. The eigenvalue and Fermi energy tolerances were set to 6.25×10^{-6} eV and 2.72×10^{-13} eV, respectively, and a smearing width of 0.1 eV was applied to facilitate convergence of the metallic states. The convergence criteria for structural relaxation were set to 0.05 eV $Å^{-1}$ for the maximum force, 0.002 Å for atomic displacement, and 0.1 GPa for the maximum stress, ensuring reliable optimization of the equilibrium structures. The optimized structures were then used to evaluate their electronic band dispersions, TDOS, and PDOS. To probe the optical behavior, the complex dielectric function was computed, which represents the interaction of photons with the electronic system across a wide energy range. Specifically, the real part, $\varepsilon_1(\omega)$, was derived utilising the Kramers–Kronig transformation, while the imaginary part, $\varepsilon_2(\omega)$, was obtained from the transition probabilities between occupied and unoccupied electronic states. Once $\varepsilon(\omega)$ was evaluated, additional optical characteristics such as the absorption coefficient, refractive index, optical conductivity, reflectivity, and energy loss function were systematically extracted.

3. Results and discussions

3.1 Structural properties and energetics of $MgBH_3$ (B = Mo, In)

The cubic perovskite hydrides $MgMoH_3$ and $MgInH_3$ crystallize in the ABX_3 structure, with Mg atoms occupying the A-site, the transition metal B (Mo, In) occupying the B-site, and hydrogen atoms forming corner-sharing BH_6 octahedra (Fig. 1). Table 1 summarizes the optimized lattice parameters (a, V), formation energies (ΔE_f), total energies (E_0), and geometric stability factors including the Goldschmidt tolerance factor (t), octahedral factor (μ), and physically based tolerance factor (τ) for $MgMoH_3$ and $MgInH_3$. The optimized lattice constants were determined

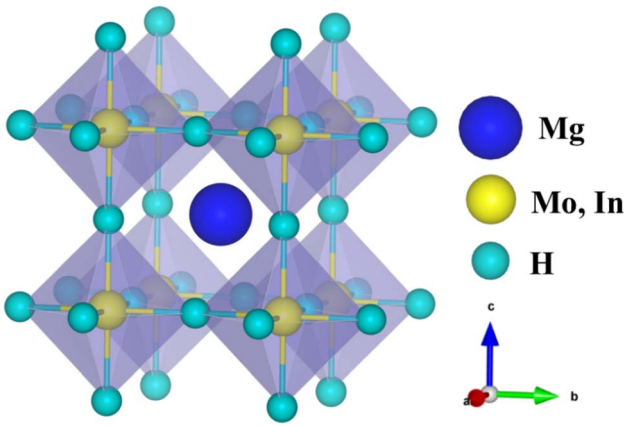

Fig. 1 Compounds unit cell of $MgBH_3$ (B = Mo and In).

through energy-volume optimization. $MgMoH_3$ exhibits a lattice parameter of 3.55 Å, corresponding to a unit cell volume of 44.72 $Å^3$, whereas $MgInH_3$ shows an expanded lattice with a lattice constant of 4.11 Å and a volume of 69.41 $Å^3$. The larger lattice of $MgInH_3$ is attributed to the greater ionic radius of In relative to Mo, leading to an expanded cubic framework.

To examine the stability of $MgMoH_3$ and $MgInH_3$ relative to competing phases, we computed their formation energies using the following equation:

$$\Delta H_f = E_{prpducts} - E_{reactance} \quad (1)$$

For the decomposition reaction of $MgBH_3$, we used the following equation:

$$MgBH_3 \rightarrow 1/2H_2 + MgH_2 + B$$

The corresponding formation enthalpy is calculated as:

$$\Delta H_f = E_{MgBH_3} - \left(\frac{1}{2}E_{H_2} + E_{MgH_2} + E_B\right) \quad (2)$$

where E_{MgBH_3} represents the total energy of the $MgBH_3$ unit cell, E_{H_2} is the energy of the hydrogen molecule, E_{MgH_2} is the energy of magnesium hydride, and E_B is the energy of B (B = Mo, In). Using this approach, the calculated formation enthalpies for $MgMoH_3$ and $MgInH_3$ are −0.769 eV/atom and −0.475 eV/atom, respectively. These values suggest that both hydrides are thermodynamically stable with respect to their competing phases. These highly negative values indicate that the formation of these hydrides from their elemental precursors is strongly exothermic, confirming their intrinsic thermodynamic stability. The total energies, −217.08 Ry for $MgMoH_3$ and −189.30 Ry for $MgInH_3$, further support the strong cohesive interactions within the lattice, reflecting robust structural integrity. For comparison, previously reported perovskite hydrides such as $MgAlH_3$ (−0.499 eV/atom), $MgScH_3$ (−0.958 eV/atom), and $MgZrH_3$ (−0.871 eV/atom)[27] show less negative formation energies, highlighting the greater intrinsic stability of $MgMoH_3$ and $MgInH_3$. Since a complete convex-hull calculation was not carried out in this study, the calculated formation enthalpies should be regarded as indicative of relative stability against the considered decomposition pathway rather than proof of absolute thermodynamic stability.

3.2 Geometric stability

The geometric stability of the cubic perovskite structure was further evaluated using the Goldschmidt tolerance factor t, octahedral factor μ, and physically based tolerance factor τ, calculated as:[28]

$$t = \frac{(R_{Mg} + R_H)}{\sqrt{2}(R_X + R_H)} \quad (3)$$

$$\mu = \frac{R_X}{R_H} \quad (4)$$

$$\tau = \frac{R_X}{R_H} - n_{Mg}\left(n_{Mg} - \frac{\frac{R_{Mg}}{R_X}}{\ln\frac{R_{Mg}}{R_X}}\right) \quad (5)$$

For cubic perovskite stability, t should fall within 0.813 to 1.107, μ within 0.37 to 0.859, and τ below 4.18. For $MgMoH_3$, the tolerance factor of 0.997 indicates near-ideal cubic packing, while the octahedral factor of 0.448 confirms that the BH_6 octahedra are appropriately coordinated. $MgInH_3$, with a slightly smaller tolerance factor of 0.949 and a higher octahedral factor of 0.519, remains within the stability range, reflecting minor lattice adjustments due to the larger B-site cation. The physically based tolerance factors for both compounds, 3.756 for $MgMoH_3$ and 3.693 for $MgInH_3$, are below the critical threshold, further confirming that the cubic perovskite structure is energetically and geometrically favorable. The calculated values are listed in Table 1.

Collectively, the combination of strongly negative formation energies, appropriate ionic packing, and favorable tolerance factors indicates that both $MgMoH_3$ and $MgInH_3$ are stable cubic hydrides. Although their gravimetric hydrogen-storage capacities remain below the DOE onboard targets, their structural robustness and moderate volumetric storage

Table 1 Structural, Thermodynamic, and Geometric Stability of Cubic $MgBH_3$ (B = Mo and In) Hydrides

Materials	a (Å)	V ($Å^3$)	ΔH_f (eV per Atom)	E_0 (Ry)	t	μ	τ
Stability criteria	—	—	$\Delta H_f < 0$	$E_0 < 0$	$0.813 < t < 1.107$	$0.37 < \mu < 0.859$	$\tau < 4.18$
$MgMoH_3$	3.55	44.72	−0.769	−217.08	0.997	0.448	3.756
$MgInH_3$	4.11	69.41	−0.475	−189.30	0.949	0.519	3.693

characteristics may still be relevant for stationary or niche hydrogen-storage applications.

3.3 Hydrogen storage performance

One of the most efficient energy carriers for stationary and transportation uses is hydrogen. Particularly in nations with limited natural resources, it provides a renewable substitute that can reduce dependency on imported petroleum.[29]

The two main processes by which hydrogen is stored in solid-state materials are physisorption and chemisorption. In chemisorption, hydrogen and the solid (usually metals) undergo a chemical process that produces hydride phases, whereas in physisorption, hydrogen molecules interact weakly with the host material through van der Waals forces.[20] In addition to the well-researched metal hydrides, recently produced perovskite-hydrides with increased hydrogen storage capacity (gravimetric density) have garnered a lot of attention.[30] The conversion of excess electrical energy into hydrogen provides a practical means of controlling power consumption and guaranteeing stability between output and consumption. Nowadays, a primary area of technical research in this area is the hunt for cutting-edge hydrogen storage materials.[31] A dependable energy management technique that allows for improved control over supply and demand fluctuations is the conversion of excess electrical output into hydrogen. Because of its technological significance, the creation of novel hydrogen storage devices is currently garnering a lot of scientific interest. One of the main obstacles to using hydrogen as fuel is the lack of materials with a sufficient gravimetric density. An integrated strategy targeted at creating and developing materials capable of achieving increased storage capacities with improved density is necessary to address this restriction.

This section focuses on assessing the hydrogen storage capacity of Mg-based perovskite hydrides, namely $MgBH_3$ (X = Mo, In). Because it measures the quantity of hydrogen that may be stored per unit mass, the gravimetric storage capacity is an important requirement. This statistic provides an exact figure that makes it easier to assess the material's overall appropriateness and efficiency for hydrogen storage applications. The gravimetric storage capacity ($C_{wt\%}$) of a hydrogen-absorbing material is generally determined by calculating the proportion between the molar mass of the absorbed hydrogen and the molar mass of the host compound.[32]

$$C_{wt\%} = \left(\frac{(H/M)m_H}{m_{host} + (H/M)m_H} \times 100\right)\% \quad (6)$$

In this equation, n is the hydrogen-to-host atomic ratio (H/M), m_H is the molar mass of hydrogen, and m_{host} is the molar mass of the host lattice. For $MgBH_3$ (B = Mo, In), calculated gravimetric hydrogen storage capacities are 2.45 wt% and 2.13 wt%, respectively. The lower capacity of $MgInH_3$ stems from the greater atomic mass of In. In general, ABH_3-type perovskite hydrides exhibit gravimetric hydrogen densities in the range of 1.2–6.0 wt%.[33] Although the hydrogen storage capacities of $MgMoH_3$ and $MgInH_3$ are moderate, they are comparable to or higher than several reported perovskite hydrides, including $RbCaH_3$,[34] $CsPtH_3$,[35] $FrPtH_3$,[35] $CsSnH_3$,[36] $FrSnH_3$,[36] $KSrH_3$,[32] $InMgH_3$,[37] $RbGaH_3$,[38] $CsGaH_3$,[38] $FrGaH_3$,[38] $CaCuH_3$,[39] $SrCuH_3$,[39] $CoCuH_3$,[40] $NiCuH_3$,[40] $ZnCuH_3$,[40] $LiNiH_3$,[41] $NaNiH_3$,[41] $KNiH_3$,[41] $CsBH_3$,[42] and $RbBH_3$.[42] These results indicate that $MgMoH_3$ and $MgInH_3$ possess competitive hydrogen-storage characteristics within the broader class of perovskite hydrides, particularly for moderate-capacity or stationary storage applications.

The thermodynamic stability of the studied hydrides was evaluated through their dehydrogenation reactions, in which molecular hydrogen (H_2) is taken as the reference state. Dehydrogenation corresponds to the release of hydrogen from the hydride upon heating and can be expressed as:

$$MgMoH_3 \rightarrow Mg + Mo + 3/2H_2$$

$$MgInH_3 \rightarrow Mg + In + 3/2H_2$$

Following the approach proposed by Ikeda,[43] the hydrogen decomposition enthalpy (ΔH) is calculated as: $\Delta H = H_{Mg} + H_{Mo} + \frac{3}{2}H_{H_2} - H_{MgBH_3}$, where H represents the total enthalpy of each system. The enthalpy is determined using: $H = E_{ele} + E_{ZPE}$. Here, E_{ele} and E_{ZPE} denote the electronic total energy and the zero-point energy, respectively. The zero-point energy is obtained from the phonon density of states as: $E_{ZPE} = \frac{\int h\omega g(\omega)d\omega}{2}$, where h, ω, and $g(\omega)$ are Planck's constant, phonon frequency, and phonon density of states, respectively. The hydrogen desorption temperature (T_{des}) is estimated using:[44] $T_{des} = -\frac{\Delta H}{\Delta S}$, where, ΔS is the entropy change of the reaction. In this work, ΔS is approximated by the entropy of hydrogen gas, taken as 130.7 J mol^{-1} K^{-1}. Using the calculated formation energies as an approximation to the decomposition enthalpy, the estimated desorption temperatures are 567 K for $MgMoH_3$ and 350 K for $MgInH_3$. These values indicate moderate thermal stability, suggesting that hydrogen release can occur at relatively accessible temperatures. Such moderate desorption temperatures are beneficial for practical hydrogen storage, as they reduce thermal stress during cycling while maintaining sufficient structural stability to prevent degradation or phase separation.

To further assess storage performance, the volumetric hydrogen storage capacity was evaluated using the relation: $\rho_{vol} = \frac{N_H \times m_H}{V(L) \times N_A}$, where, N_H is the number of hydrogen atoms per formula unit, m_H is the mass of a hydrogen atom, V is the unit cell volume, and N_A is Avogadro's number. The calculated volumetric hydrogen storage capacities are 112 kg m^{-3} for $MgMoH_3$ and 72 kg m^{-3} for $MgInH_3$. The higher volumetric capacity of $MgMoH_3$ arises from its smaller lattice parameter and more compact crystal structure, which allows denser hydrogen packing. In contrast, the larger ionic radius of In leads to lattice expansion in $MgInH_3$, resulting in reduced volumetric storage density. These results highlight a clear trade-off between atomic size and hydrogen packing efficiency, where

smaller B-site elements favour enhanced volumetric storage performance.

Although $MgMoH_3$ and $MgInH_3$ exhibit moderate volumetric hydrogen-storage capacities and favorable structural stability, their gravimetric storage capacities remain below the U.S. Department of Energy (DOE) onboard hydrogen-storage target. In addition, practical hydrogen-storage performance may also be influenced by factors such as hydrogen desorption kinetics, reversibility, and equilibrium hydrogen pressure, which were not explicitly investigated in the present study.[45–47] Therefore, the current work should be regarded as a theoretical assessment of the structural stability, hydrogen-storage behavior, and physical properties of $MgBH_3$ (B = Mo, In) hydrides. Experimental validation is encouraged to confirm the predicted stability and hydrogen-storage characteristics of these compounds. Furthermore, the hydrogen-storage performance may potentially be improved through elemental doping, defect engineering, or nanostructuring approaches, which could enhance surface activity and hydrogen adsorption/desorption kinetics compared with bulk materials.[48–51]

3.4 Mechanical properties

Revealing the mechanical stability of materials is crucial for harnessing their full potential in real-time applications. The elastic constants C_{11}, C_{12}, and C_{44} for $MgMoH_3$ and $MgInH_3$ are reported in Table 2, revealing a robust and stable material that meets the stringent Born stability criteria for cubic crystals: $C_{11} - C_{12} > 0$, $C_{11} + 2C_{12} > 0$, $C_{44} > 0$, confirming that both compounds are mechanically stable.[45] Specifically, $MgMoH_3$ shows $C_{11} - C_{12} = 212.52$ GPa and $C_{44} = 36.72$ GPa, while $MgInH_3$ exhibits higher longitudinal stiffness ($C_{11} - C_{12} = 73.02$ GPa) but lower shear resistance ($C_{44} = 9.22$ GPa).

The mechanical response of a material is characterized by its stiffness coefficients, adding longitudinal stiffness (C_{11}), transverse stiffness (C_{12}), and shear stiffness (C_{44}). Table 2 represents the computed properties, consisting of bulk moduli and shear moduli, derived through the Voigt, Reuss, and Hill methods. The values present in Table 2 are derived using the Hill method, offering a reliable estimate of the material's mechanical behavior. The mechanical properties of $MgBH_3$ (B = Mo, In) have been thoroughly investigated by computing the Voigt and Reuss bulk moduli (B_V and B_R), shear moduli (G_V and G_R), Young's modulus (E), Poisson's ratio (ν), and elastic anisotropy (A). The computed values are presented in Table 3 and are determined using the following formulas:[44]

$$B_V = \frac{1}{3}(C_{11} + 2C_{12}) \quad (7)$$

$$G_V = \frac{1}{5}(C_{11} - C_{12} + 3C_{44}) \quad (8)$$

$$B_R = B_V = \frac{1}{3}(C_{11} + 2C_{12}) \quad (9)$$

$$G_R = \frac{5C_{44}(C_{11} - C_{12})}{[4C_{44} + 3(C_{11} - C_{12})]} \quad (10)$$

The overall bulk modulus (B) and shear modulus (G) are then calculated as the arithmetic mean of the Voigt and Reuss values, in accordance with Hill's theory:[52]

$$B = \frac{1}{2}(B_v + B_R) \quad (11)$$

$$G = \frac{1}{2}(G_v + G_R) \quad (12)$$

In addition, Young's modulus (E) and Poisson's ratio (ν) are determined using:[53]

$$Y = \frac{9BG}{3B + G} \quad (13)$$

$$\nu = \frac{(3B - 2G)}{2(3B + G)} \quad (14)$$

The bulk moduli of the two hydrides differ significantly: $MgMoH_3$ exhibits $B = 117.09$ GPa, whereas $MgInH_3$ has $B = 47.54$ GPa, showing a disparity of about 59%. This indicates that $MgMoH_3$ is considerably more resistant to uniform compression than $MgInH_3$, meaning the two compounds will respond differently to pressure variations during hydrogenation cycles. In contrast, their resistance to shape deformation also shows notable variations. The shear modulus decreases from $G = 57.14$ GPa for $MgMoH_3$ to $G = 16.65$ GPa for $MgInH_3$, a reduction of nearly 71%, while the Young's modulus drops from 147.44 GPa to 44.73 GPa (around 70%). Thus, although $MgMoH_3$ maintains greater rigidity, $MgInH_3$ is mechanically softer with lower shear and tensile stiffness.

Poisson's ratio (ν) is an important mechanical parameter for identifying both the bonding type and the ductile or brittle nature of a material. Typically, $\nu \approx 0.10$ corresponds to covalent bonding, $\nu \approx 0.25$ to ionic, and $\nu \approx 0.33$ to metallic bonding.[43] In addition, $\nu = 0.26$ is often taken as the dividing line between brittle ($\nu < 0.26$) and ductile ($\nu > 0.26$) behavior.[44] For $MgMoH_3$ ($\nu = 0.29$) and $MgInH_3$ ($\nu = 0.34$), the values are above the ductility threshold and fall within or above the metallic regime, suggesting significant metallic bonding contributions and ductile characteristics. Another useful indicator is Pugh's ratio (B/G),

Table 2 Elastic Constants and moduli of compound $MgBH_3$ (B = Mo and In) hydrides

Compounds	C_{11} (GPa)	C_{12} (GPa)	C_{44} (GPa)	B (GPa)	G (GPa)	Y (GPa)
$MgMoH_3$	258.77	46.25	36.72	117.09	57.14	147.44
$MgInH_3$	96.22	23.20	9.22	47.54	16.65	44.73

Table 3 Mechanical indicators of $MgBH_3$ (B = Mo, In) hydrides

Compounds	ν	B/G	C_P (GPa)	A	μ_m	H_V (GPa)	Mechanical nature
$MgMoH_3$	0.29	2.05	9.53	0.40	3.19	6.12	Ductile, metallic bonding, moderate anisotropy, good hardness
$MgInH_3$	0.34	2.85	13.98	0.79	5.16	2.89	Softer, highly ductile, metallic bonding, strong anisotropy

where values greater than 1.75 denote ductility, while values below 1.75 correspond to brittleness.[52] Both hydrides satisfy this criterion, confirming their ductile nature. The inverse ratio (G/B), with values of 0.34 for $MgMoH_3$ and 0.26 for $MgInH_3$, lies well below the typical covalent (~1.1) and ionic (~0.6) benchmarks, further supporting their metallic-like bonding behavior.[53] Cauchy pressure ($C_P = C_{12} - C_{44}$) provides additional insight: positive values indicate ionic/metallic bonding and ductility, whereas negative values point to covalent and brittle characteristics. Both $MgMoH_3$ (9.58 GPa) and $MgInH_3$ (13.98 GPa) exhibit positive C_P, again consistent with ductile metallic bonding.

The elastic anisotropy factor, defined as $A = \frac{2C_{44}}{C_{11} - C_{12}}$, is a critical parameter for distinguishing isotropic ($A = 1$) from anisotropic ($A \neq 1$) materials. The computed value is $A = 0.40$ for $MgMoH_3$ and $A = 0.79$ for $MgInH_3$. These hydride perovskites are mechanically anisotropic, as evidenced by the large deviations of both values from unity. A more unequal distribution of bonding stiffness across crystallographic orientations is reflected in the higher deviation in $MgInH_3$, which suggests a greater directional dependency of its elastic response.

The machinability index $\mu_M = B/C_{44}$, gauges intrinsic plasticity and workability (higher $\mu_M \Rightarrow$ easier machining (values $\gtrsim 1$ are considered workable)).[54,55] High workability is indicated by $MgMoH_3$'s $\mu_M = 3.19$ and $MgInH_3$'s $\mu_M = 5.16$, while lower shear resistance is reflected by $MgInH_3$'s greater value. In contrast to $MgMoH_3$, which strikes a compromise between moderate shear rigidity and increased tensile strength for better structural integrity, $MgInH_3$ is softer and more compliant due to its higher shear rigidity but lower tensile resistance. Both machinability index values of both investigated materials are higher than those of $LiPH_3$ (1.29), $NaPH_3$ (1.62), and KPH_3 (1.63),[56] and $AClH_3$ (A = Rb, Cs, K: 1.45, 1.32, 1.56),[57] verifying their excellent flexibility and fabrication capabilities. This improved machinability is particularly beneficial for hydrogen storage, as it reduces microcrack formation.

The Vickers hardness, estimated using the relation $H_v = \frac{(1-2\nu)Y}{6(1+\nu)}$, measures a material's resistance to plastic deformation and serves as an indicator of the mechanical durability of hydrogen storage compounds. The calculated hardness for $MgMoH_3$ is 6.12 GPa, whereas $MgInH_3$ has 2.89 GPa. The soft-to-moderately hard domain ($H_V < 10$ GPa)[41] is where these hydride perovskites fall for both values, which is advantageous for preserving structural integrity and preventing excessive brittleness during hydrogen cycling. When compared with other reported hydride perovskites, such as $MgCuH_3$ (0.77 GPa), $RbNiH_3$ (0.64 GPa), $BeGaH_3$ (3.02 GPa), and $BeInH_3$ (3.17 GPa),[58] both $MgGaH_3$ and $MgTlH_3$ show significantly higher hardness values, underscoring their enhanced mechanical stability. In hydrogen storage applications, this enhanced hardness and ductility (shown by $B/G > 1.75$) imply that these compounds can withstand microcrack development and structural deterioration, guaranteeing dependable cycle performance.

3.5 Electronic properties

To comprehend a material's electronic properties, it is essential to look at its electronic band structure and density of states. The vertical axis of these figures represents the energy levels, while the horizontal axis traces the wave vector (k) along specific high-symmetry areas in the Brillouin zone (BZ). Fig. 2, 3 displays the total density of states (DOS) and calculated electronic band structures for the cubic phases along the high-symmetry path X–M–R–Γ–R. The reference between the valence and conduction bands is the Fermi level, which is represented by a dashed line at 0 eV. The energy range in which the electronic band structures are shown is −4 to +4 eV. After the structural optimization, the electrical characteristics of $MgBH_3$ (B = Mo, In) were investigated using first-principles calculations. The band structures of the studied compounds are depicted in Fig. 2 and 3, and the lack of a band gap verifies that the lowest unoccupied and highest occupied electronic states are not separated in energy. According to this, electrons can easily move from the valence band to the conduction band, confirming the metallic nature of these perovskite hydrides and boosting to their excellent electrical conductivity.[59] Comparable electronic configurations have been observed in other magnesium-based perovskites, with previous studies consistently reporting metallic behavior.[60] In agreement with these findings, our investigation of $MgBH_3$ (B = Mo, In) also demonstrates a comparable electronic structure, further confirming their metallic nature.

The TDOS and PDOS for $MgBH_3$ (B = Mo, In) at zero temperature and pressure are displayed in Fig. 3. Mg-p, Mo-p/d, and H-p orbitals primarily control the conduction and valence bands in $MgMoH_3$, whereas Mg-s/p, In-p/d, and H-p orbitals dominate the contributions in $MgInH_3$, as seen in Fig. 3. These states play a crucial role in determining the electrical characteristics of these hydrides because most of them are found in the energy range of −3 eV to +5 eV. The PDOS analysis reveals pronounced p-d hybridization between the H-p orbitals and the Mo/In-p, d or Mg-s, p orbitals in both $MgMoH_3$ and $MgInH_3$.

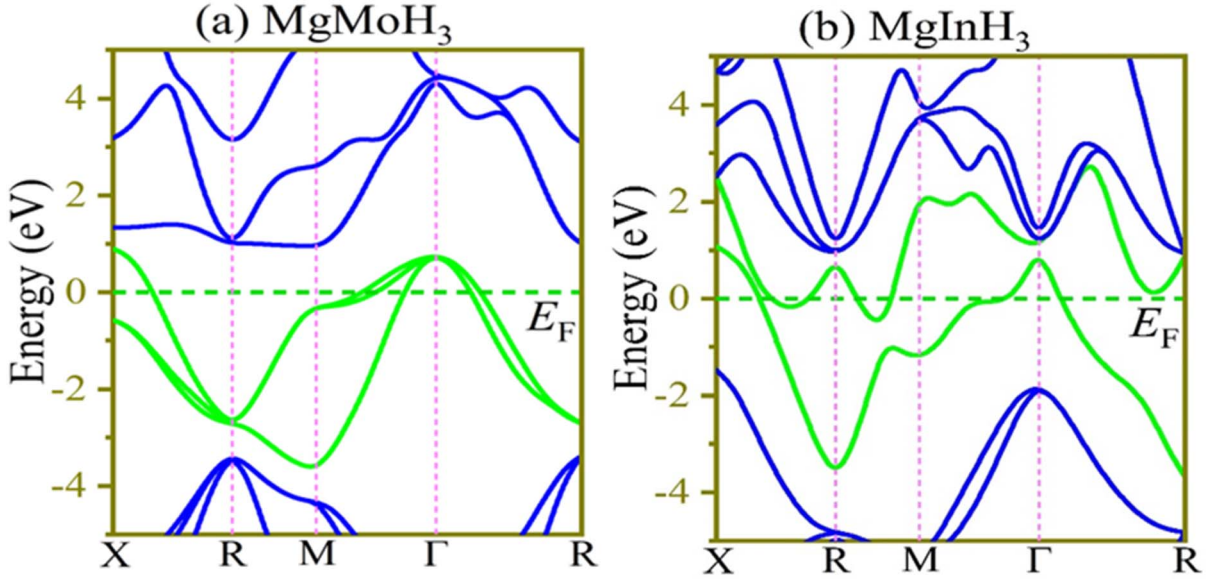

Fig. 2 Band diagram of $MgBH_3$ (a) $MgMoH_3$, (b) $MgInH_3$ hydrides.

This strong orbital interaction signifies substantial covalent bonding, contributing to the electronic stability of these perovskite hydrides. Additionally, $MgInH_3$ exhibits a slightly higher density of states near the Fermi level compared to $MgMoH_3$, suggesting enhanced electronic conductivity and more efficient charge carrier mobility.

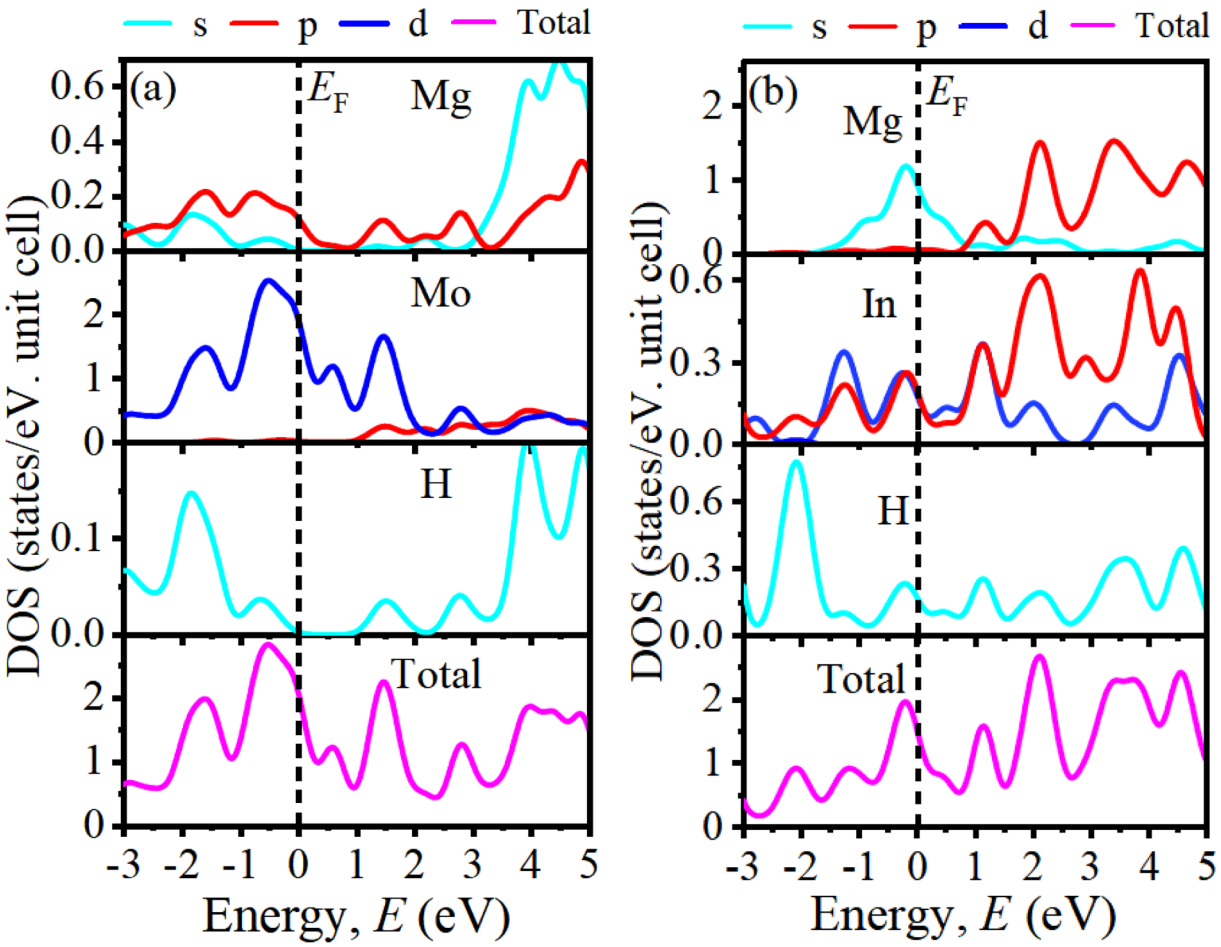

Fig. 3 Compounds partial density of states (a) $MgMoH_3$, (b) $MgInH_3$ hydrides.

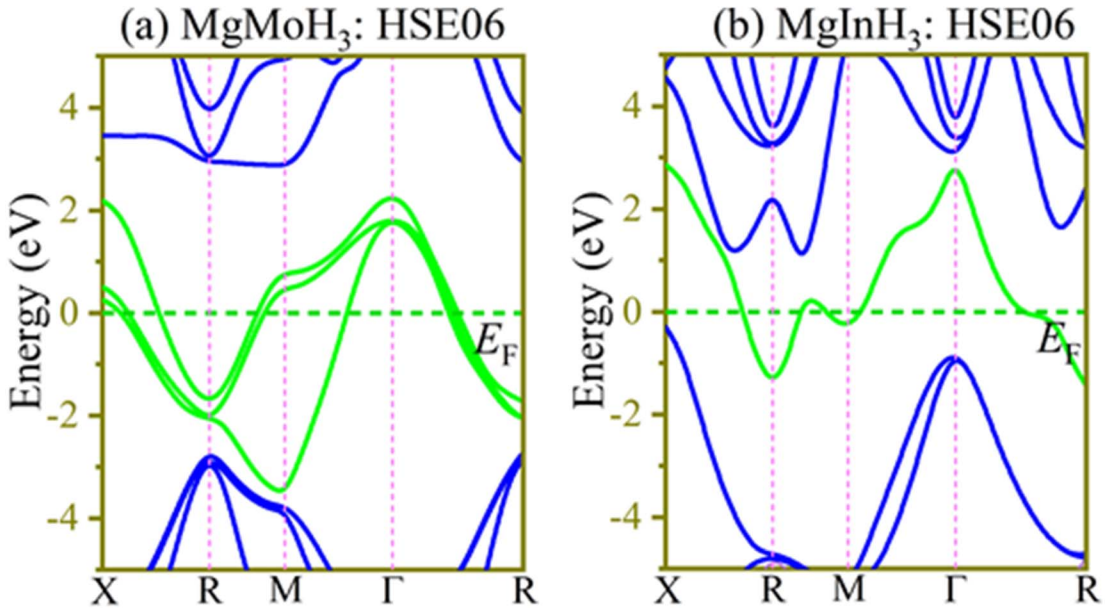

Fig. 4 Electronic band structures of (a) $MgMoH_3$ and (b) $MgInH_3$ calculated using the HSE06 hybrid functional along the high-symmetry directions (X–R–M–Γ–R).

The electronic band structures of $MgMoH_3$ and $MgInH_3$ were further evaluated using the hybrid HSE06 functional to improve the accuracy of exchange-correlation effects, particularly near the Fermi level. The calculated HSE06 band structures, shown in Fig. 4a and b, reveal that both compounds retain their metallic character, as evidenced by the absence of a band gap and the clear overlap between valence and conduction bands at the Fermi level ($E_F = 0$ eV). For $MgMoH_3$, multiple bands cross the Fermi level along the high-symmetry directions (X–R–M–Γ–R), indicating a high density of itinerant charge carriers and strong electronic conductivity. The dispersion of bands near E_F suggests significant hybridization between Mo-d and H-p states, which facilitates electron mobility. Similarly, $MgInH_3$ exhibits band crossings at the Fermi level, confirming its metallic nature. However, compared to $MgMoH_3$, the bands near E_F appear relatively less dispersive in certain regions, implying slightly different carrier dynamics and orbital contributions, likely arising from the In-p/d states interacting with H-p orbitals.

Importantly, the use of the HSE06 functional provides more reliable electronic structure predictions than standard GGA. The results confirm that the metallic behavior is intrinsic and not an artifact of the exchange–correlation approximation. This metallic nature is beneficial for hydrogen storage, as it promotes efficient charge transfer. It may also enhance hydrogen adsorption and desorption kinetics.

3.6 Optical properties

In this study, the optical properties of $MgBH_3$ (B = Mo, In) were systematically investigated over a photon energy range up to 12 eV. The analysis focused on several key parameters, including the absorption coefficient ($\alpha(\omega)$), photoconductivity ($\sigma(\omega)$), reflectivity ($R(\omega)$), real and imaginary components of the dielectric function ($\varepsilon(\omega)$), energy-loss function ($L(\omega)$), extinction coefficient ($k(\omega)$), and refractive index ($n(\omega)$). Examining these frequency-dependent optical properties provides a comprehensive understanding of the electronic transitions and light-matter interactions in these compounds.

The optical behavior of a material is governed by its interaction with incident electromagnetic radiation and provides important insight into its dielectric and metallic response characteristics. This is described by the complex dielectric function, $\varepsilon(\omega) = \varepsilon_1(\omega) + i\varepsilon_2(\omega)$, following Ehrenreich and Cohen. Here, ω is the angular frequency, $\varepsilon_1(\omega)$ represents the real part obtained *via* the Kramers–Kronig relation, reflecting the induced polarization, while $\varepsilon_2(\omega)$, derived from Kohn–Sham electronic transitions,[9] indicates the material's absorption of incoming radiation.

$$\varepsilon_1(\omega) = 1 + \frac{2}{\pi} p \int_0^{\alpha_{\omega' \times \varepsilon_2(\omega')}} \frac{}{\omega'^2 - \omega^2} \mathrm{d}\omega \tag{15}$$

$$\varepsilon_2(\omega) = \frac{2\pi e^2}{\Omega \varepsilon_0} \sum_{k,v,c} \left| \langle \Psi_k^c | \hat{u} \times \vec{r} | \Psi_k^v \rangle \right|^2 \delta(E_k^c - E_k^v - E) \tag{16}$$

In the first expression, p denotes the primary parameter. Conversely, the second relation introduces the terms v, e, h, p, k_n, and k_n which correspond to the crystal cell volume, elementary electric charge, reduced Planck's constant, momentum transition operator, valence-band wave function, and conduction-band wave function, respectively. Accurate evaluation of these optical parameters is vital for improving the performance of electronic and optoelectronic devices. In the low-energy region, the imaginary part $\varepsilon_2(\omega)$ of the dielectric function decreases sharply with increasing photon energy (Fig. 5b), indicating a reduced probability of interband electronic transitions, as $\varepsilon_2(\omega)$ directly reflects photon absorption *via* electronic excitations.[61] Conversely, the real part $\varepsilon_1(\omega)$ of the

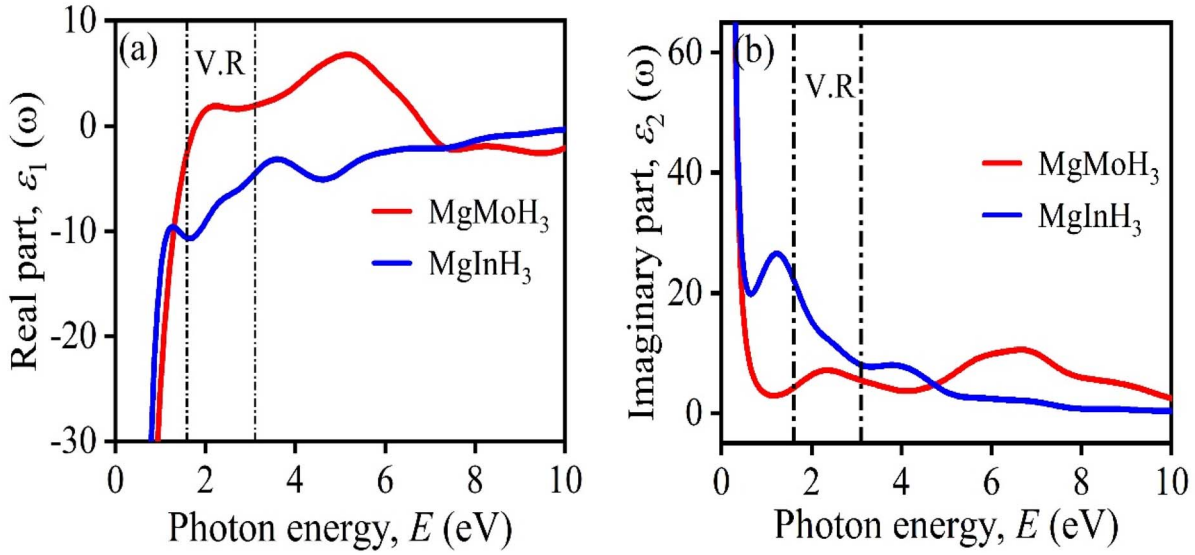

Fig. 5 Compounds $MgBH_3$ (B = Mo, In) dielectric function (a) $\varepsilon_1(\omega)$ and (b) $\varepsilon_2(\omega)$.

dielectric function rises notably in this energy range, reflecting increased polarization and charge displacement within the lattice under an external electric field. Both $MgMoH_3$ and $MgInH_3$ exhibit high static dielectric constants, indicating strong interaction with incident electromagnetic radiation and pronounced dielectric response characteristics associated with their metallic electronic structure. In the UV region, the imaginary part $\varepsilon_2(\omega)$ approaches zero, indicating negligible absorption at higher energies. This suggests minimal dielectric loss, consistent with the metallic behavior observed in the band structure and DOS analyses, thus supporting the theoretical predictions. Another important feature occurs in the high-energy (UV) region, where the $\varepsilon_1(\omega)$ and $\varepsilon_2(\omega)$ curves intersect and the dielectric constant approaches unity. This marks the critical transition at which the material becomes transparent to incident electromagnetic radiation, allowing photons above this energy to pass through with minimal attenuation. This high-energy transparency reflects reduced photon absorption in the ultraviolet region and highlights the distinct dielectric and optical response characteristics of these metallic hydrides at higher photon energies. Furthermore, these optical characteristics underline the importance of Mg-based hydrides as candidate materials for multifunctional applications. The high dielectric response at low photon energies reflects strong polarization behavior, while the reduced absorption at higher photon energies highlights the characteristic metallic and dielectric optical response of these hydrides across a broad energy range.

From the calculated values of $\varepsilon_1(\omega)$ and $\varepsilon_2(\omega)$ a range of optical responses was determined, such as the complex refractive index, optical conductivity (real part), absorption spectrum, reflectivity, and the electron energy loss spectrum. The refractive index was expressed in its complex form as $n(\omega) - ik(\omega)$, where $n(\omega)$ denotes the real component associated with light propagation, and $k(\omega)$ refers to the extinction coefficient describing attenuation within the medium. These quantities were systematically obtained using standard relations and widely adopted theoretical expressions.[62,63]

$$n(\omega) = \frac{1}{\sqrt{2}}\left\{\sqrt{\varepsilon_1^2(\omega) + \varepsilon_2^2(\omega)} + \varepsilon_1(\omega)\right\}^{\frac{1}{2}} \quad (17)$$

$$k(\omega) = \frac{1}{\sqrt{2}}\left\{\sqrt{\varepsilon_1^2(\omega) + \varepsilon_2^2(\omega)} - \varepsilon_1(\omega)\right\}^{\frac{1}{2}} \quad (18)$$

$$I(\omega) = \sqrt{2}\omega\left\{\sqrt{\varepsilon_1^2(\omega) + \varepsilon_2^2(\omega)} + \varepsilon_1(\omega)\right\}^{\frac{1}{2}} \quad (19)$$

$$R(\omega) = \frac{\{n(\omega) - 1\}^2 + k^2(\omega)}{\{n(\omega) + 1\}^2 + k^2(\omega)} \quad (20)$$

The refractive index $n(\omega)$ is an important optical parameter that governs the propagation of electromagnetic radiation through a material and provides valuable insight into its dielectric and optical response characteristics. Since the real component of $\Delta(\omega)$ characterizes the degree of light refraction at the interface between various media, and it is associated with the transparency of the material. As shown in Fig. 6a, the refractive index at 0 eV exceeds 10 for both $MgMoH_3$ and $MgInH_3$. In the infrared region, the refractive index first reaches a maximum, then slightly decreases, and rises again in the visible region. Across the visible spectrum, the values gradually decline from about 2.62 to 1.50 for $MgInH_3$ and 1.29 to 1.96 for $MgMoH_3$. In the ultraviolet range, $\Delta(\omega)$ continues to fall, approaching nearly zero, which is lower than silicon nitride (~1.9).[64]

One important metric that reacts to the amount of light absorption and scattering in a material is the extinction coefficient $k(\omega)$; higher values indicate stronger absorption of the

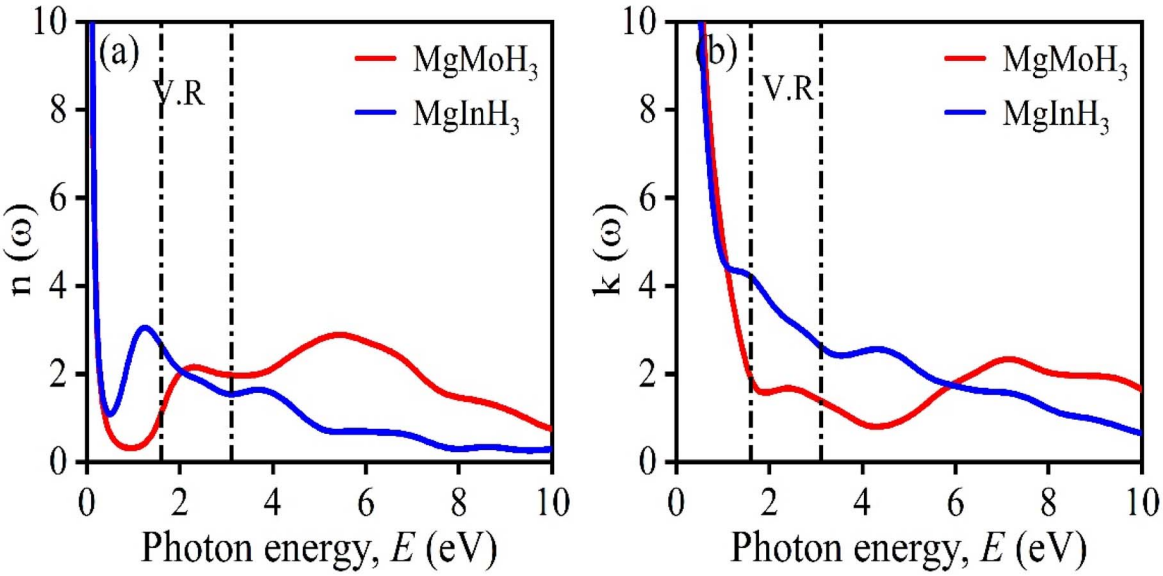

Fig. 6 Optical parameters of $MgBH_3$ (B = Mo, In): (a) refractive index and (b) extinction coefficient.

incoming radiation. As shown in Fig. 6b, both $MgMoH_3$ and $MgInH_3$ exhibit their maximum extinction in the infrared region. In the visible spectrum, the extinction coefficient decreases, ranging from 4.00 to 2.54 for $MgInH_3$ and 1.60 to 1.30 for $MgMoH_3$, indicating a moderate reduction in absorption strength. In the ultraviolet region, the extinction coefficient approaches zero, reflecting reduced absorption at higher photon energies and the characteristic energy-dependent optical response of these metallic hydrides.

Optical conductivity reflects a material's ability to absorb photons and generate charge transport under electromagnetic excitation, offering key insights into free-electron contribution and its relation to reflectivity. At zero energy, the conductivity is high, but it decreases with increasing photon energy in the infrared region. For $MgInH_3$, conductivity rises again from the infrared to the visible range, showing prominent peaks above 4.36 Ω^{-1} cm^{-1} in the infrared. In contrast, $MgMoH_3$ exhibits a steady increase from the infrared to the ultraviolet, with its strongest peaks in the UV region, reaching values above 8.58 Ω^{-1} cm^{-1}. At higher photon energies, the conductivity continues to decline and eventually approaches zero, consistent with the weakening photon absorption. Interestingly, the spectra also exhibit wave-like oscillations (rise-fall features) as a function of energy, reflecting the interplay of interband transitions and the availability of electronic states. This behavior, presented in Fig. 7a, confirms the strong optical response of these hydrides in the lower-energy domain while indicating reduced conductivity in the ultraviolet regime.

Optical reflectivity, $R(\omega)$, represents the fraction of incoming photons reflected from the surface of the crystal. As shown in Fig. 7b, its spectral trend is inversely related to the absorption curve, displaying clear variations with photon energy. At zero photon energy, both $MgMoH_3$ and $MgInH_3$ exhibit high static reflectivity values of approximately 0.98. With increasing photon energy, the reflectivity decreases from the infrared to visible region before increasing again in the ultraviolet range.

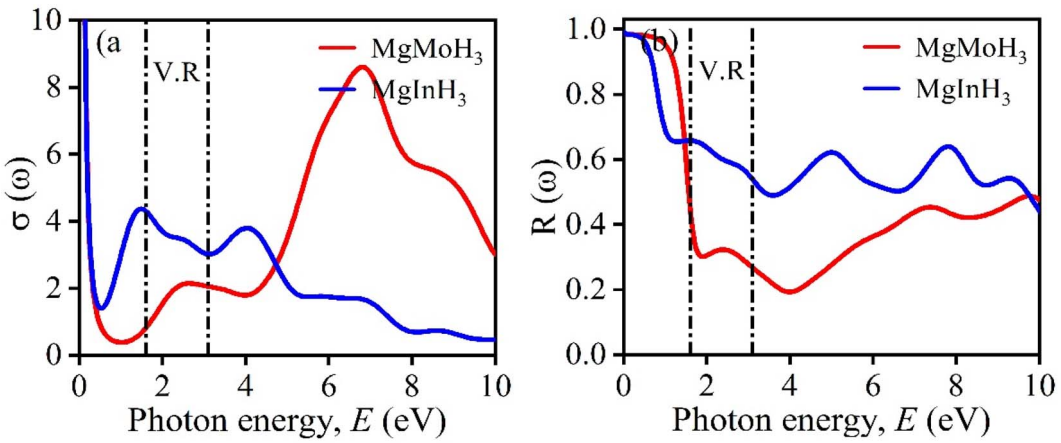

Fig. 7 The optical response of $MgBH_3$ (X = Mo, In) showing (a) optical conductivity and (b) reflectance.

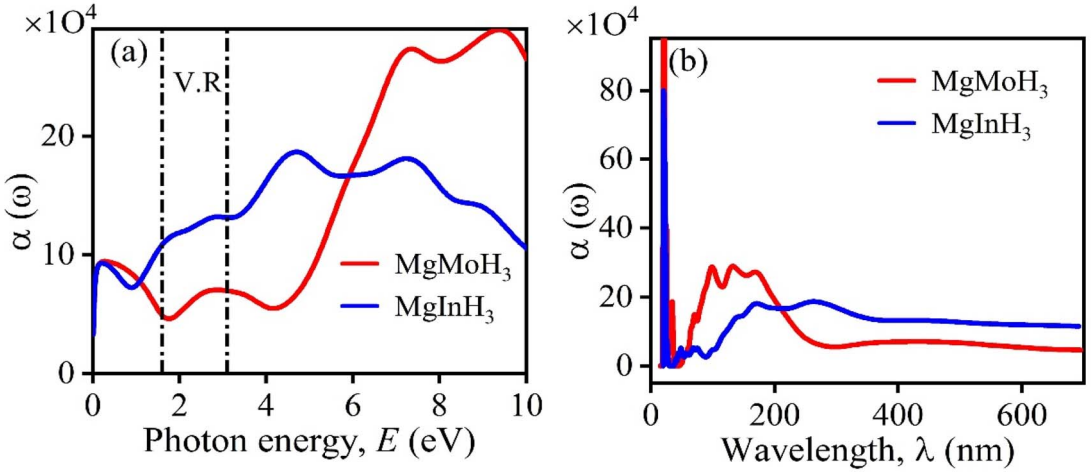

Fig. 8 Optical response of $MgBH_3$ (B = Mo, In): (a) absorption coefficient (eV) and (b) absorption coefficient (nm).

This oscillatory behavior originates from interband electronic transitions and variations in the dielectric response of the materials. The combination of high refractive index and characteristic reflectivity behavior further reflects the distinct metallic and dielectric optical response of these hydrides.

The mathematical expression for absorption coefficient $\alpha(\omega)$ is obtained by combining the real and imaginary contributions of the dielectric response, which allows accurate estimation of a material's photon absorption capability across the studied energy spectrum.[65]

$$\alpha(\omega) = 2\omega\left(\frac{\left[\varepsilon_1^2(\omega) + \varepsilon_2^2(\omega)\right]^{1/2} - \varepsilon_1(\omega)}{2}\right)^{1/2} \quad (21)$$

Visible-range absorption (1.6 to 3.2 eV, 780 to 380 nm) is especially important to solar and light-driven devices. For the compounds studied, the initial absorption peak appears in the infrared region, with $MgInH_3$ showing about 10.55×10^4 cm^{-1} at 1.50 eV and $MgMoH_3$ about 9.22×10^4 cm^{-1} at 0.50 eV. With increasing photon energy, absorption rises again within the IR domain. In the visible range, $MgMoH_3$ exhibits values of 4.00×10^4 to 6.00×10^4 cm^{-1}, while $MgInH_3$ ranges between 11.22×10^4 and 13.50×10^4 cm^{-1}. A continuous increase in the absorption coefficient is observed as the photon energy shifts toward the ultraviolet (UV) region, where both compounds attain their maximum absorption strengths. $MgMoH_3$ reaches a peak value of 28.85×10^4 cm^{-1} at 9.50 eV, while $MgInH_3$ exhibits a maximum value of 18.65×10^4 cm^{-1} at 4.66 eV, as shown in Fig. 8a. These high absorption coefficients indicate strong photon-electron interactions and efficient electromagnetic energy absorption over a broad energy range. Their strong electronic response may still be relevant for understanding energy-transfer processes that could influence hydrogen adsorption/desorption kinetics under external thermal or electromagnetic stimulation.

3.7 Thermodynamic properties

Debye temperature (Θ_D) is the temperature at which wavelength of phonons approaches the lattice parameter of the unit cell, and the limit between low- and high-temperature behavior of solids. Debye temperature is a characteristic parameter as the materials with higher Θ_D will have stronger atomic bonding, higher melting points, increased hardness, increased velocity of propagation of acoustic waves, and lower mean atomic weights. Debye temperature is estimated from the average sound velocity (v_m), which may be calculated using both shear modulus and bulk modulus.

$$v_m = \left[\frac{1}{3}\left(\frac{2}{v_t^3} + \frac{1}{v_l^3}\right)\right]^{-\frac{1}{3}} \quad (22)$$

In formula 22, v_t corresponds to the transverse acoustic velocity, while v_l represents the longitudinal acoustic velocity. These sound velocities can be obtained using the following expressions.

$$v_l = \left(\frac{B + \frac{3}{4}G}{\rho}\right) \quad \text{and } v_t = \left[\frac{G}{\rho}\right]^{\frac{1}{2}} \quad (23)$$

The Debye temperature (Θ_D)[66] can be determined using the following mathematical relation:

$$\Theta_D = \frac{h}{k_B}\left[\frac{3n}{4\pi V_0}\right]^{1/3} v_m \quad (24)$$

The expression is here h being Planck's constant, k_B the Boltzmann constant, V_0 is the unit-cell volume, n the number of atoms in the unit cell, and v_m the average sound velocity. The Debye temperatures were calculated as 565.32 K and 307.91 K for $MgMoH_3$ and $MgInH_3$, respectively (Table 4). These compounds possess lower Θ_D and therefore expand more gradually on being heated and endure thermal stress, thereby becoming potential candidates for thermal barrier coatings (TBCs) on various substrates.

Thermal conduction in crystalline solids is mainly conducted through vibrational motion of the lattice ions, known as lattice thermal conductivity (κ_{ph}). For the estimation of such a property, Slack's empirical relation[67] was employed, a usual

Table 4 Calculated thermodynamic and thermal transport parameters

Compound	ρ (g cm^{-3})	v_t (km s^{-1})	v_l (km s^{-1})	v_m (km s^{-1})	θ_D (K)	T_m (K)	k_{ph} (W m^{-1} K^{-1})	γ	k_{min} (W m^{-1} K^{-1})
$MgMoH_3$	4.578	3.533	6.498	3.941	565.32	2082.33	11.14	1.71	1.26
$MgInH_3$	3.401	2.213	4.529	2.486	307.91	1121.66	1.68	2.05	0.59

method to estimate phonon-conducted thermal conductivity in semiconductors and perovskite complex compounds.

$$\kappa_{ph} = A(\gamma)\frac{M_{av}\theta_D^3\delta}{\gamma^2 n^{\frac{2}{3}}T} \quad (25)$$

Based on this model, lattice thermal conductivities (κ_{ph}) of the studied perovskites hydrides are 11.14 W m^{-1} K^{-1} for $MgMoH_3$ and 1.68 W m^{-1} K^{-1} for $MgInH_3$, as shown in Table 4. $MgInH_3$'s smaller κ_{ph} indicates more phonon scattering, which could be due to the heavier atomic mass and larger unit-cell distortions of In, while $MgMoH_3$'s larger value offers more efficient phonon transport. These results are consistent with other perovskites, *e.g.*, lead-halide $MAPbI_3$ possessing ultralow κ_{ph} (0.5 to 1.0 W m^{-1} K^{-1}) at RT due to anharmonicity and lattice softness,[67] highlighting the varied thermal behavior in perovskite families.

The Grüneisen parameter (γ) is a well-known thermal descriptor that quantifies lattice anharmonicity and is extremely widely used in solid-state physics to evaluate how the lattice vibrations respond to stress or volumetric changes. Higher values of γ are indicators of greater anharmonicity, affecting thermal expansion, phonon scattering, and heat transport. For $MgBH_3$ (B = Mo, In), γ is calculated by applying Poisson's ratio,[66] providing a quantitative measure of anharmonic behavior and phonon scattering in such hydride perovskites [eq. (26)].

$$\gamma = \frac{3(1+v)}{2(2-3v)} \quad (26)$$

The Grüneisen parameter (γ) quantifies lattice anharmonicity and its influence on thermal properties. For the studied hydride perovskites, γ values calculated are 1.71 for $MgMoH_3$ and 2.05 for $MgInH_3$ (Table 4). The calculated values are in line with typical solids, which usually show $\gamma \approx 2.0$,[66] indicating average anharmonic influences in the lattice.

Measurement of minimum thermal conductivity (K_{min}) is most important for applications at high temperatures because K_{min} is the most easily accessible thermal conductivity at high temperatures. Vacancies or dislocations in the structure have no effect on K_{min}, because phonon wavelengths at high temperatures approach the interatomic distance. Average sound velocity and Debye temperature are intrinsic properties which determine mainly K_{min} and influence temperature-dependent thermal properties and electrical conductivity. For the studied compounds, K_{min} was calculated using Clarke's model[65] eqn (27), which considers the average sound velocity, molecular weight, density, and atomic packing.

$$k_{min} = k_B v_a \left(\frac{M}{n\rho N_A}\right)^{-2/3} \quad (27)$$

The calculated minimum thermal conductivity (k_{min}) values for $MgMoH_3$ and $MgInH_3$ are 1.26 W m^{-1} K^{-1} and 0.59 W m^{-1} K^{-1}, respectively, as summarized in Table 4. Materials with higher Debye temperatures and greater average sound velocities tend to exhibit increased k_{min} values. Therefore, an enhancement in either Debye temperature or sound velocity is generally associated with a rise in the minimum thermal conductivity of the material, highlighting its thermal transport efficiency under high-temperature conditions.

4. Conclusion

In the current work, structural, electronic, optical, mechanical, and thermodynamic properties of double hydride perovskites $MgBH_3$ (B = Mo, In) have been investigated using density functional theory in detail. The two compounds have been found to be stable thermodynamically with negative formation energies and positive tolerance and octahedral factors. Theoretical hydrogen-storage analysis indicates moderate gravimetric and competitive volumetric storage capacities together with moderate desorption temperatures, suggesting potential relevance for stationary or niche hydrogen-storage applications. Electronic structure analysis confirms the metallic nature of these hydrides, while the calculated high optical absorption ($\sim 10^4$ cm^{-1}) reflects strong photon interaction and dielectric/metallic optical response characteristics. From the mechanical viewpoint, the hydrides are tough with ductile character and high elastic anisotropy, suggesting robustness under operating conditions. Thermodynamic analysis: Debye temperature, melting point, lattice and minimum thermal conductivity, and Grüneisen parameter reflect efficient conduction of heat, suggesting applicability in high-temperature technologies such as thermal barrier coatings. The calculated results suggest that $MgBH_3$ (B = Mo, In) hydrides possess stable structural frameworks, ductile mechanical behavior, moderate hydrogen-storage capacity, and distinct dielectric/metallic optical responses. This work expands the current theoretical understanding of Mg-based hydride perovskites and may guide future studies on multifunctional hydride materials.

Author contributions

Md. Shahazan Parves: writing manuscript-reviewing and editing. Md. Hasan Mia: conceptualization; methodology; writing manuscript-reviewing and editing; data curation; validation; supervision Omar Alsalmi: formal analysis, data curation, review-editing Md. Zahid Hasan: formal analysis; validation; review-editing; and supervision.

Conflicts of interest

The authors declare that they have no known conflicting financial interests or personal ties that may have seemed to affect the work presented in this study.

Data availability

Relevant data from this study are available from the corresponding author upon a reasonable request.

Acknowledgements

The authors extend their appreciation to Umm Al-Qura University, Saudi Arabia, for funding this research work through grant number: 26UQU4300099GSSR02. Funding statement: this research work was funded by Umm Al-Qura University, Saudi Arabia under grant number: 26UQU4300099GSSR02.

References

1 I. A. Hassan, H. S. Ramadan, M. A. Saleh and D. Hissel, Hydrogen storage technologies for stationary and mobile applications: Review, analysis and perspectives, *Renew. Sustain. Energy Rev.*, 2021, **149**, 111311.
2 L. Zhou, Progress and problems in hydrogen storage methods, *Renew. Sustain. Energy Rev.*, 2005, **9**, 395–408.
3 M. R. Raupach, *et al.*, Global and regional drivers of accelerating CO_2 emissions, *Proc. Natl. Acad. Sci. U. S. A.*, 2007, **104**(24), 10288–10293, DOI: 10.1073/pnas.0700609104.
4 A. Gencer, G. Surucu and S. Al, $MgTiO_3Hx$ and $CaTiO_3Hx$ perovskite compounds for hydrogen storage applications, *Int. J. Hydrogen Energy*, 2019, **44**(23), 11930–11938.
5 W. Hao and J. Xie, Reducing diffusion-induced stress of bilayer electrode system by introducing pre-strain in lithium-ion battery, *J. Electrochem. Energy Convers. Storage*, 2021, **18**(2), 020909.
6 A. Kojima, K. Teshima, Y. Shirai and T. Miyasaka, Organometal halide perovskites as visible-light sensitizers for photovoltaic cells, *J. Am. Chem. Soc.*, 2009, **131**(17), 6050–6051.
7 H. Zhou, Q. Chen, G. Li, S. Luo, T.-B. Song, H.-S. Duan, Z. Hong, J. You, Y. Liu and Y. Yang, Interface engineering of highly efficient perovskite solar cells, *Science*, 2014, **345**(6196), 542–546.
8 Z. X. Guo, C. Shang and K. F. Aguey-Zinsou, Materials challenges for hydrogen storage, *J. Eur. Ceram. Soc.*, 2008, **28**(7), 1467–1473.
9 J. Zheng, C.-G. Wang, H. Zhou, E. Ye, J. Xu, Z. Li and X. J. Loh, Current research trends and perspectives on solid-state nanomaterials in hydrogen storage, *Research*, 2021, **2021**, 3750689.
10 N. A. Ali, M. S. Yahya, N. Sazelee, M. F. M. Din and M. Ismail, Influence of nanosized $CoTiO_3$ synthesized via a solid-state method on the hydrogen storage behavior of MgH_2, *Nanomaterials*, 2022, **12**(17), 3043.
11 D. P. Broom, Potential storage materials, in *Hydrogen Storage Materials: The Characterisation of Their Storage Properties*, Springer, London, 2011, pp. 19–59.
12 L. Kong and G. Liu, Synchrotron-based infrared microspectroscopy under high pressure: An introduction, *Matter Radiat. Extremes*, 2021, **6**(6), 068202.
13 M. Kaur and K. Pal, Review on hydrogen storage materials and methods from an electrochemical viewpoint, *J. Energy Storage*, 2019, **23**, 234–249.
14 R. K. Ahluwalia, X. Wang, A. Rousseau and R. Kumar, Fuel economy of hydrogen fuel cell vehicles, *J. Power Sources*, 2004, **130**(1–2), 192–201.
15 S.-H. Ri, U.-G. Jong, T.-S. Im and U.-R. Rim, Perovskite-type hydrides $ACaH_3$ (A = Li, Na): computational investigation on materials properties for hydrogen storage applications, *RSC Adv.*, 2025, **15**, 19245–19253.
16 P. Ahmadi and E. Kjeang, Realistic simulation of fuel economy and life cycle metrics for hydrogen fuel cell vehicles, *Int. J. Energy Res.*, 2017, **41**(5), 714–727.
17 Q. Sun, N. Wang, Q. Xu and J. Yu, Nanopore-supported metal nanocatalysts for efficient hydrogen generation from liquid-phase chemical hydrogen storage materials, *Adv. Mater.*, 2020, **32**(44), 2001818.
18 X. Zhang, Y. Tang, F. Zhang and C.-S. Lee, A novel aluminum–graphite dual-ion battery, *Adv. Energy Mater.*, 2016, **6**(11), 1502588.
19 E. Rivard, M. Trudeau and K. Zaghib, Hydrogen storage for mobility: a review, *MDPI*, 2019, **12**(12), 1973.
20 H. Jiang, Z. Ding, Y. Li, G. Lin, S. Li, W. Du, Y. Chen, L. L. Shaw and F. Pan, Hierarchical interface engineering for advanced magnesium-based hydrogen storage: synergistic effects of structural design and compositional modification, *Chem. Sci.*, 2025, **16**(18), 7610–7636.
21 G. Surucu, A. Gencer, A. Candan, H. H. Gullu and M. Isik, $CaXH_3$ (X = Mn, Fe, Co) perovskite-type hydrides for hydrogen storage applications, *Int. J. Energy Res.*, 2020, **44**, 2345–2354.
22 M. K. Shahzad, S. Hussain, M. N. Khan, M. J. Aslam, R. M. Mohammed, V. Tirth, H. Alqahtani, A. Algahtani, T. Al-Mughanam and W. Azeem, Computational insights of double perovskite Na_2CaCdH_6 hydride alloy for hydrogen storage applications: a DFT investigation, *Sci. Rep.*, 2024, **14**(1), 25102.
23 A. Siddique, *et al.*, Structures and hydrogen storage properties of $AeVH_3$ (Ae= Be, Mg, Ca, Sr) perovskite hydrides by DFT calculations, *Int. J. Hydrogen Energy*, 2023, **48**(63), 24401–24411.
24 J. P. Perdew, K. Burke and M. Ernzerhof, Generalized Gradient Approximation Made Simple, *Phys. Rev. Lett.*, 1996, **77**(18), 3865–3868, DOI: 10.1103/PhysRevLett.77.3865.
25 J. P. Perdew, *et al.*, Generalized gradient approximation for solids and their surfaces, *Phys. Rev. Lett.*, 2008, **100**(13), 136406, DOI: 10.1103/PhysRevLett.100.136406.
26 T. H. Fischer and J. Almlof, General methods for geometry and wave function optimization, *J. Phys. Chem.*, 1992, **96**(24), 9768–9774, DOI: 10.1021/j100203a036.

27 S. Bahhar, A. Tahiri, A. Jabar, M. Louzazni, M. Idiri and H. Bioud, Computational assessment of $MgXH_3$ (X= Al, Sc and Zr) hydrides materials for hydrogen storage applications, *Int. J. Hydrogen Energy*, 2024, **58**, 259–267.

28 C. Li, X. Lu, W. Ding, L. Feng, Y. Gao and Z. Guo, Formability of abx_3 (x= f, cl, br,i) halide perovskites, *Struct. Sci.*, 2008, **64**(6), 702–707.

29 B. Sakintuna, F. Lamari-Darkrim and M. Hirscher, Metal hydride materials for solid hydrogen storage: a review, *Int. J. Hydrogen Energy*, 2007, **32**(9), 1121–1140.

30 P. Schouwink, *et al.*, Structure and properties of complex hydride perovskite materials, *Nat. Commun.*, 2014, **5**(1), 5706.

31 D. P. Broom, The accuracy of hydrogen sorption measurements on potential storage materials, *Int. J. Hydrogen Energy*, 2007, **32**(18), 4871–4888.

32 H. H. Raza, G. Murtaza, U. Hani, N. Muhammad and S. M. Ramay, First-principle investigation of $XSrH_3$ (X = K and Rb) perovskite-type hydrides for hydrogen storage, *Int. J. Quantum Chem.*, 2020, **120**(24), e26419.

33 K. Ikeda, T. Sato and S. Orimo, Perovskite-type hydrides–synthesis, structures and properties, *Int. J. Mater. Res.*, 2008, **99**(5), 471–479.

34 H. Murtaza, Q. Ain, A. Kumar, A. M. Ali, A. D. Oza and J. Munir, The Effect of Pressure in Tuning the Optoelectronic, Thermoelectric and Hydrogen Storage Properties of $RbCaH_3$ for Renewable Energy Applications, *J. Energy Storage*, 2025, **134**, 118183.

35 A. Bakar, H. Muhammad, M. Ahmed, M. S. Kiani, A. Quader, S. Batay and H. Elhosiny Ali, Investigations for hydrogen storage applications of $XPtH_3$ (X= Cs, Fr) hydrides: A first principles study, *Chem. Phys.*, 2025, **591**, 112566.

36 M. K. Masood, W. Khan, K. Chaoui, Z. Ashraf, S. Bibi, A. Kanwal, A. A. Alothman and J. Rehman, Theoretical investigation of $XSnH_3$ (X: Rb, Cs, and Fr) perovskite hydrides for hydrogen storage application, *Int. J. Hydrogen Energy*, 2024, **63**, 1248–1257.

37 M. Hadhoud, O. Eddahmani, A. El Mekkaouy, A. Tahiri and R. Touti, Indium-Based Perovskite Hydrides $InZH_3$ (Z = Be, Ca, Mg) as Promising Hydrogen Storage Materials: A Comprehensive First-Principles Study, *Int. J. Hydrogen Energy*, 2026, **231**, 154842.

38 R. M. Khalil, S. Hayat, M. I. Hussain, A. M. Rana and F. Hussain, DFT based first principles study of novel combinations of perovskite-type hydrides $XGaH_3$ (X= Rb, Cs, Fr) for hydrogen storage applications, *AIP Adv.*, 2021, **11**(2), 025032.

39 B. Ahmed, M. B. Tahir, A. Ali and M. Sagir, First-principles screening of structural, electronic, optical and elastic properties of Cu-based hydrides-perovskites $XCuH_3$ (X= Ca and Sr) for hydrogen storage applications, *Int. J. Hydrogen Energy*, 2024, **54**, 1001–1007.

40 S. Hayat, R. M. A. Khalil, M. I. Hussain, A. M. Rana and F. Hussain, First-principles investigations of the structural, optoelectronic, magnetic and thermodynamic properties of hydride perovskites $XCuH_3$ (X= Co, Ni, Zn) for hydrogen storage applications, *Optik*, 2021, **228**, 166187.

41 A. Gencer and G. Surucu, Investigation of structural, electronic and lattice dynamical properties of $XNiH_3$ (X= Li, Na and K) perovskite type hydrides and their hydrogen storage applications, *Int. J. Hydrogen Energy*, 2019, **44**(29), 15173–15182.

42 B. Ahmed, M. B. Tahir, S. Nazir, M. Alzaid, A. Ali, M. Sagir and A. Hussein, An Ab-initio simulation of boron-based hydride perovskites XBH_3 (X= Cs and Rb) for advance hydrogen storage system, *Comput. Theor. Chem.*, 2023, **1225**, 114173.

43 M. Baaddi, R. Chami, O. Baalla, S. El Quaoubi, S. Ali, L. El H. Omari and M. Chafi, The effect of strain on hydrogen storage characteristics in K_2NaAlH_6 double perovskite hydride through first principle method, *Environ. Sci. Pollut. Res.*, 2024, **31**(53), 62056–62064.

44 Md Hasan Mia, Md Shahazan Parves, O. Alsalmi and Md Z. Hasan, Investigating Stability, Thermomechanical, Optoelectronic, and Hydrogen Storage Potential of $MgXH_3$ (X= Ga, Tl) Perovskites via DFT and AIMD Simulations, *ACS Appl. Eng. Mater.*, 2025, **3**(11), 4218–4232.

45 L. Charpin and A. Ehrlacher, Estimating the Poroelastic Properties of Cracked Materials, *Acta Mech.*, 2014, **225**(9), 2501–2519.

46 B. Ahmed, M. B. Tahir, M. Sagir, A. Parveen, Z. Abbas and A. A. Nassani, First-Principles Study of Ti-Based X_2TiH_5 (X= Mg, Ca, Sr) Hydrides for Advanced Hydrogen Storage Applications, *Chem. Phys.*, 2025, **589**, 112499.

47 Md H. Mia, Md Rasheduzzaman, O. Alsalmi and Md Z. Hasan, Theoretical Investigation of Gravimetric Capacity, Magnetic Behavior, and Stability of $CsAH_3$ (A= Fe, Cu, and Tl) Hydrides via DFT and DFT-Based AIMD Simulations, *Int. J. Hydrogen Energy*, 2026, **209**, 153607.

48 A. Manzoor, M. A. Ullah, M. W. Yasin, S. S. A. Gillani, M. Ikram and M. Rizwan, Investigation $SrLiF_3$-xHx Perovskites through Ion Replacement Mechanism for Advance Solid Hydrogen Storage Systems: A Prediction through DFT-Based Calculations, *J. Energy Storage*, 2024, **88**, 111639.

49 M. Rizwan, H. F. Arooj, F. Noor, K. Nawaz, M. A. Ullah, Z. Usman, A. Ali and T. Mahmood, Computational Study to Investigate Effectiveness of Titanium Substitution in $CaFeH_3$ Perovskite-Type Hydride: An Approach towards Advanced Hydrogen Storage System, *J. Mater. Res. Technol.*, 2024, **31**, 2676–2684.

50 M. A. Ullah, K. N. Riaz and M. Rizwan, Computational Evaluation of $KMgO_3$-xHx as an Efficient Hydrogen Storage Material, *J. Energy Storage*, 2023, **70**, 108030.

51 D. P. Broom, C. J. Webb, G. S. Fanourgakis, G. E. Froudakis, P. N. Trikalitis and M. Hirscher, Concepts for Improving Hydrogen Storage in Nanoporous Materials, *Int. J. Hydrogen Energy*, 2019, **44**(15), 7768–7779.

52 F. Mouhat and F.-X. Coudert, Necessary and sufficient elastic stability conditions in various crystal systems, *Phys. Rev. B*, 2014, **90**(22), 224104, DOI: 10.1103/PhysRevB.90.224104.

53 R. Hill, The elastic behaviour of a crystalline aggregate, *Proc. Phys. Soc., London, Sect. A*, 1952, **65**(5), 349.

54 I. R. Shein and A. L. Ivanovskii, Elastic properties of mono- and polycrystalline hexagonalAlB_2-like diborides of s, p and d metals from first-principles calculations, *J. Phys.: Condens. Matter*, 2008, **20**(41), 415218.
55 I. N. Frantsevich, *Elastic Constants and Elastic Moduli of Metals and Insulators*, 1982.
56 Z. Sun, D. Music, R. Ahuja and J. M. Schneider, Theoretical investigation of the bonding and elastic properties of nanolayered ternary nitrides, *Phys. Rev. B*, 2005, **71**(19), 193402, DOI: 10.1103/PhysRevB.71.193402.
57 D. V. Suetin, I. R. Shein and A. L. Ivanovskii, Elastic and electronic properties of hexagonal and cubic polymorphs of tungsten monocarbide WC and mononitride WN from first-principles calculations, *Phys. Status Solidi B*, 2008, **245**(8), 1590–1597, DOI: 10.1002/pssb.200844077.
58 H. Murtaza, Q. Ain, S. A. Issa, H. M. Zakaly and J. Munir, A precise prediction for the hydrogen storage ability of perovskite XPH_3 (X= Li, Na, K) hydrides: First-principles study, *Int. J. Hydrogen Energy*, 2024, **94**, 1084–1093.
59 H. Murtaza, S. M. Qaid, H. M. Ghaithan, A. A. A. Ahmed and J. Munir, The excellent performance of $AClH_3$ (A= Rb, Cs, K) perovskite hydrides for hydrogen storage applications, *Renewable Energy*, 2025, **252**, 123491.
60 W. Khan and M. K. Masood, The investigation of rubidium-based hydrides for hydrogen storage application: density functional theory study, *Mater. Sci. Semicond. Process.*, 2024, **173**, 108149.
61 W. Kuang, H. Wang, X. Li, J. Zhang, Q. Zhou and Y. Zhao, Application of the thermodynamic extremal principle to diffusion-controlled phase transformations in Fe-CX alloys: Modeling and applications, *Acta Mater.*, 2018, **159**, 16–30.
62 H. Ehrenreich and H. R. Philipp, Optical Properties of Ag and Cu, *Phys. Rev.*, 1962, **128**(4), 1622–1629, DOI: 10.1103/PhysRev.128.1622.
63 D. N. Basov, R. D. Averitt and D. Hsieh, Towards properties on demand in quantum materials, *Nat. Mater.*, 2017, **16**(11), 1077–1088.
64 A. V. Zayats, I. I. Smolyaninov and A. A. Maradudin, Nano-optics of surface plasmon polaritons, *Phys. Rep.*, 2005, **408**(3–4), 131–314.
65 M. Irfan, E. M. Ahmed, S. A. M. Issa and H. M. H. Zakaly, New eco-friendly lead-free double perovskites Rb_2FeCdO_6 driven semiconducting material for radiation shielding and energy applications: DFT + U based nanoarchitectonics, *Opt. Quant. Electron.*, 2024, **56**(8), 1355, DOI: 10.1007/s11082-024-07263-0.
66 R. Sa, Y. Wei, W. Zha and D. Liu, A first-principle study of the structural, mechanical, electronic and optical properties of vacancy-ordered double perovskite Cs_2TeX_6 (X= Cl, Br, I), *Chem. Phys. Lett.*, 2020, **754**, 37538.
67 M. Tarekuzzaman, M. S. Parves, M. Z. Rahman and S. S. Hasan, Cesium-Based Perovskite Hydrides: A Theoretical Insight into Hydrogen Storage and Optoelectronic Characteristics, *Solid State Commun.*, 2025, **404**, 116043.